A two-scale model of degenerated graphite in cast iron

R. Rizzoni*, P. Livieri, R. Tovo

ᵃDepartment of Engineering, University of Ferrara, Via Saragat 1, 44122 Ferrara, Italy

Abstract. A two-scale model for clusters of degenerated graphite in gray cast iron is presented. The novelty of the model is that, at the mesoscale, a single cluster is described as a spheroidal inclusion made of porous materials. At the microscale, the porous material contains a random distribution of randomly oriented spheroidal voids modeling the graphite precipitates. To calculate the stress state inside and at the outer surface of the cluster, two different approaches are presented. In the first approach, the effective elastic properties of the porous material at the microscale are obtained using Pan and Weng homogenization scheme, based on Eshelby's equivalent principle and the Mori-Tanaka's estimate; at the mesoscale, the stress distributions inside and at the outer surface of the cluster are calculated using Eshelby's solution applied to an inclusion made of equivalent porous material. The second approach is based on a finite element analysis of a cluster embedding 216 randomly oriented and randomly distributed spheroidal voids. A comparison between the numerical results obtained with the two approaches indicates good agreement in terms of average (elastic and stress distribution) properties. The equivalent elastic properties (Young's modulus) calculated at the microscale in the two approaches are also compared with some experimental results available in the scientific literature.

Keywords: Spheroidal cast iron, degenerated graphite; cluster; elastic plate; spheroidal voids; porous material; effective elastic moduli; spheroidal inclusion; stress analysis; multiscale method.

1. Introduction

Due to its good mechanical properties, such as machinability, strength, fatigue and wear resistance, spheroidal cast iron has a wide range of engineering applications in turbines, pipes, machines, and automotive industry parts. In the scientific literature, spheroidal cast iron is often viewed as a composite material in which graphite nodules, acting as reinforcement, are dispersed into a metallic matrix. Following this idea, many studies focus on damage and failure of such a material. A typical modeling approach is to study spheroidal graphite particles regularly embedded into a metallic matrix [1,2,3]. The graphite particles are often modelled as voids or cavities, due to their early decohesion from the matrix, cf. [2,4,5].

In spheroidal graphite cast iron, higher graphite nodularity results in higher ductility and strength but deviations from the spherical shape frequently occur. Degenerated graphite precipitates with complex microstructures may form in the casting under certain circumstances, resulting in a deterioration of the mechanical properties, cf. [6,7,8,9,10,11] and references therein.

Gray cast iron is intrinsically characterized by the presence of multiple scales: the macroscale of the sample, the mesoscale at the level of clusters of degenerated graphite and the microscale at the level of graphite precipitates. Macroscale mechanical models are usually built up on constitutive phenomenological relations, in which descriptors of the microstructure such as orientation, size, shape or alignment distributions are unaccounted for, so this kind of models may be not accurate enough. At the meso- and microscale, the morphology of graphite clusters and the three-dimensional microstructure of graphite precipitates are usually very complex for a FE analysis, requiring too much computational effort. Therefore, a multiscale approach is a reasonable compromise between accuracy, complexity and computational time.

The most detrimental forms of graphite, lamellar or spiky graphite precipitates, often tend to aggregate into clusters that can be viewed as another material phase, i.e. a mixture of graphite particles and metal matrix. Based on this idea, a multiscale description of the mechanical behavior of degenerated graphite clusters has been provided in [12,13]. The main simplifying assumption in these two studies is that graphite particles and their aggregates can be described as elliptical or spheroidal voids and inclusions. This assumption allows to exploit the well-known analytical methods for composites relying upon the equivalent inclusion method of Eshelby [14,15,16] and on its mean field extensions, cf. [17,1819,20,21] and the references therein. On the other hand, degenerated graphite particles occurring in elongated, needle-like shape are best fitted by ellipses and ellipsoids with large aspect ratio. In [12], the interaction of two clusters modeled as two elliptical voids

---

in an infinite plate under tensile loading is studied. In [13], a multiscale approach is proposed for the description of the behavior of degenerated graphite bidimensional clusters viewed as an aggregate of elliptical voids dispersed into a linear elastic, isotropic bidimensional matrix.

In the present work, we propose an original generalization of the study in [13] to the three-dimensional case. At the microscale, i.e. the scale of graphite precipitates, we follow [2,4,5] in assuming that the precipitates can be described as spheroidal voids, due to the observed early decohesion from the matrix. In addition, the voids are assumed to be randomly oriented and randomly distributed in an elastic isotropic matrix. In Section 2, we apply the Pan and Weng homogenization scheme [22] to calculate the effective properties of the porous equivalent material. There exists an extensive literature on both analytical and computational homogenization models, for a recent state of art review see [23]. Here, we follow the approach proposed by Tandon and Weng [24,25,26] and further specialized by Pan and Weng to the case of spheroidal voids [22]. The advantage of this homogenization scheme, combining Eshelby's theory and Mori–Tanaka's method, is that it gives a closed form solution for finite concentrations of ellipsoidal inclusions with a wide range of inclusion aspect ratios. As the aspect ratio of the inclusions changes, the effective moduli calculated with the Tandon and Weng homogenization scheme are shown to vary within the Hashin-Shtrikman bounds [26]. In other homogenization methods, as the self-consistent method, the generalized self-consistent method, and the differential method, the shapes of the inclusions are limited to spheres and short fibers, cf. [23] and references therein. The effective elastic properties obtained using the Tandon and Weng homogenization scheme are then compared with those calculated via a finite element analysis performed in COMSOL Multiphysics on distributions of randomly oriented spheroidal voids randomly distributed in an elastic isotropic matrix. At the mesoscale, i.e. the scale of a cluster of graphite precipitates, Eshelby's fundamental solution [14,15,16] is used to calculate the stress distributions internal and external to the cluster, assumed to be composed of the equivalent porous material. In Section 3, the (uniform) internal stress components are then compared with the average internal stress components calculated with the finite element method inside a reference spheroidal surface containing the spheroidal voids. A similar comparison is performed between the averaged stress components at the outer surface of the inclusion with porous materials and the analogous ones calculated using the finite element analysis at the reference spheroidal surface. The stress distribution analysis is also applied to obtain stress concentration factors inside and at the outer surface of the cluster. Section 4 is devoted to a comparison between the effective elastic properties predicted by the two approaches, homogenization and finite element modeling, and some experimental results available in the scientific literature for materials with random distributed porosity. Results and concluding remarks are summarized in Section 5, along with some comments on possible future developments.

2. Microscale modelling

Cast iron is naturally a two-phase material: iron containing graphite inclusions. These can be modeled as spheroidal inclusions randomly distributed in a three-dimensional isotropic infinite matrix. The inclusions can be assumed randomly oriented, the composite being macroscopically isotropic.

Several methods can be envisaged for the analysis of the average properties of such a composite. Here, two different approaches are followed: an analytical one proposed in [22,24,25,26] and based on Eshelby's formalism, and a finite element (FE) analysis performed with COMSOL Multiphysics commercial finite element code.

2.1. Homogenization approach

The average elastic properties of the composite and the elastic stress distribution in and around the spheroidal inclusions at finite concentration can be analyzed via the homogenization approach proposed by Tandon and Weng, based on Eshelby's equivalent principle and Mori- Tanaka's concept of average stress in the matrix. A detailed exposition of this approach can be found in [24,25] for aligned inclusions and in [26] for randomly oriented inclusions. Results for effective elastic constants of randomly oriented ellipsoidal

voids are given in [22]. In particular, in the Pan and Weng (PW) estimate the effective bulk and shear moduli, $\bar{\kappa}$ and $\bar{\mu}$ respectively, are found to depend on the void volume fraction λ and on the elasticity coefficient of the matrix, κ and μ according to the following:

$$\bar{\kappa} = \frac{\kappa}{1+p\frac{\lambda}{1-\lambda}} \tag{1}$$

$$\bar{\mu} = \frac{\mu}{1+q\frac{\lambda}{1-\lambda}} \tag{2}$$

the constants p and q depending on the components of the Eshelby's tensor, S_{ijkl}, as follows:

$$\begin{aligned} p = -\frac{1}{3A}[&(-S_{1111} + S_{1122} + 1)(S_{2233} - S_{3333} + 1) \\ &+ (-S_{1111} + S_{1133} + 1)(-S_{2222} + S_{3322} + 1) \\ &+ (-S_{1122} + S_{1133} + 1)(S_{2211} - S_{3311}) + S_{2211}(S_{3322} - S_{3333}) \\ &+ (1 - S_{2222})(S_{3311} - S_{3333} + 1) + S_{2233}(S_{3311} - S_{3322}) + S_{3311})], \end{aligned} \tag{3}$$

$$\begin{aligned} q = (1/(15\,A))[&(1 - S_{1111})\,(2\,S_{2222} + S_{2233} + S_{3322} + 2\,S_{3333} - 4) \\ &+ S_{2211}\,(2\,S_{1122} + S_{1133} - S_{3333} + 1) \\ &+ S_{3311}\,(S_{1122} + 2\,S_{1133} + S_{2233}) + S_{1122}\,(S_{2233} - S_{3333} + 1) \\ &+ S_{3322}\,(S_{1133} + S_{2211} + 2\,S_{2233}) \\ &+ (1 - S_{2222})\,(S_{1133} + S_{3311} + 2\,S_{3333} - 2)] \\ &+ (1/5)\,(1/(1 - 2\,S_{1212}) + 1/(1 - 2\,S_{1313}) + 1/(1 - 2\,S_{2323})), \end{aligned} \tag{4}$$

with

$$\begin{aligned} A = (S_{3333} - 1)\,(&(S_{1111} - 1)\,(S_{2222} - 1) - S_{1122}\,S_{2211}) \\ &- S_{3322}\,((S_{1111} - 1)\,S_{2233} - S_{1133}\,S_{2211}) \\ &- S_{3311}\,(S_{1133}\,(S_{2222} - 1) - S_{1122}\,S_{2233}). \end{aligned} \tag{5}$$

The components of the Eshelby's tensor, S_{ijkl}, depend on the ellipsoid's semi-axis aspect ratio t (the ratio of length to diameter) as specified in the Appendix.

Given $\bar{\kappa}$ and $\bar{\mu}$ as in Equations (1) and (2), the average Young modulus, $\bar{E}$, and average Poisson ratio, $\bar{\nu}$, can be calculated using the following standard relations:

$$\bar{E} = \frac{9\bar{\kappa}\,\bar{\mu}}{3\bar{\kappa}+\bar{\mu}}, \qquad\qquad \bar{\nu} = \frac{3\bar{\kappa}-2\,\bar{\mu}}{2\,(3\bar{\kappa}+\bar{\mu})}. \tag{6}$$

When the spheroidal voids have an aspect ratio $t \to \infty$, the voids are geometrically equivalent to cracks. In this limit case, the effective Young's modulus and Poisson ratio given by Equations (6) and (7) reduce to the following simple forms:

$$\bar{E}_c = \frac{15\,E\,(1-\lambda)}{15+4\lambda(5+\nu-4\nu^2)}, \tag{7}$$

$$\bar{\nu}_c = \frac{15\nu+\lambda(5-3\nu-8\nu^2)}{15+4\lambda(5+\nu-4\nu^2)}, \tag{8}$$

where E and ν are the Young's modulus and Poisson's ratio of the matrix, respectively, related to κ and μ as in Equations (6). For spherical voids, Weng [W] has calculated the following equivalent moduli:

$$\bar{E}_s = -\frac{2E_0(\lambda-1)(5\nu-7)}{15\lambda\nu^2+2(\lambda+5)\nu-13\lambda-14}, \tag{9}$$

$$\bar{\nu}_s = \frac{5(\lambda+2)\nu^2+2(\lambda-7)\nu-3\lambda}{15\lambda\nu^2+2(\lambda+5)\nu-13\lambda-14}. \tag{10}$$

The simplest estimate for the effective elastic behavior of a porous material with porosity λ is given by the classical rule of mixtures (RM):

$$E_{mix} = E\,(1-\lambda), \tag{11}$$

$$\nu_{mix} = \nu\,(1-\lambda). \tag{12}$$

In Section 2.3, the average elastic properties evaluated using (1)-(6) and (11)-(12) are compared with the results of the FE analysis described in the next Subsection.

2.2. Finite element analysis

A three-dimensional finite element analysis has been performed with commercially available software (COMSOL Multiphysics). The matrix is assumed to be elastic isotropic with Young's modulus $E = 206$ GPa and Poisson's ratio $\nu = 0.3$. The graphite inclusions are modeled as voids dispersed in the matrix. Two different microstructures have been examined: an ordered distribution of voids and a disordered distribution of voids. In the ordered distribution, 216 randomly oriented voids are placed at the centers of a uniform grid with cube elementary cells of $1\times1\times1$ mm. The union of $6\times6\times6$ elementary cells gives the cube of Figure 1. In the disordered distribution, the centers of the voids are placed randomly inside the volume without overlapping by using a random sequential adsorption model, as shown in Figure 1b.

The number of 216 voids was inspired by the bidimensional analysis conducted in previous paper [13], where the microstructural texture was approximated by means of about 200 ordered and disordered 2D voids in a rectangular plate. The reason behind the choice of the disordered distribution, in addition to the ordered one, is to take into account a more general random microstructure, i.e. to consider randomness not only in the orientation of the spheroids but also in their positions. Undoubtedly, the choice of two different distributions adds more generality to the analysis.

In both types of voids distributions, the internal voids are ellipsoids of revolution with semi-axis aspect ratio t ranging between 0.1 and 0.8 and size of major axis ranging between 0.05 and 0.45 millimeters, implying a porosity ranging between $5\cdot10^{-6}$ up to 0.24. The orientation angle of each ellipsoid was randomly evaluated for a discrete uniform distribution by means of a commercial numeric computing environment. After the generation, it has been verified that the average distribution of each angle was around zero. Figures 1c and 1d show the typical mesh used in the numerical analysis where quadratic elements have been used. The example is relative to ellipsoidal voids with semi axis of $0.4\times0.16\times0.16$ millimeter. In the reported example the number of elements were around $5\cdot10^5$.

The boundary conditions applied to the model take inspiration from tensile tests on porous specimens, like the ones experimentally characterized in [30]. The average elastic properties have been calculated by prescribing a uniform tensile stress σ_n applied along the z direction at $z = L$, while simultaneously prescribing the displacement boundary conditions shown schematically in Figure 2. The average displacements in the z direction Δu_z at the surface $z = L$, the average displacements Δu_x in the x direction at the free surface $x = L$, and the Δu_y in the y direction at the free surface $y = L$ have been evaluated numerically. The effective Young's modulus along the z direction and the Poisson's ratios in the x and y direction have been calculated as $\bar{E}_z = \sigma_n/(\Delta u_z/L)$, $\bar{\nu}_{zx} = -(\Delta u_x/L)/(\Delta u_z/L)$ and $\bar{\nu}_{zy} = -(\Delta u_y/L)/(\Delta u_z/L)$, respectively. Analogous results have been obtained by prescribing uniform tensile stresses σ_n applied along the x and the y directions. For a stress applied along the x (y) direction, the Young's modulus $\bar{E}_x$ ($\bar{E}_y$) and the Poisson ratios $\bar{\nu}_{xy}$ ($\bar{\nu}_{yx}$) and $\bar{\nu}_{xz}$ ($\bar{\nu}_{yz}$) have been calculated.
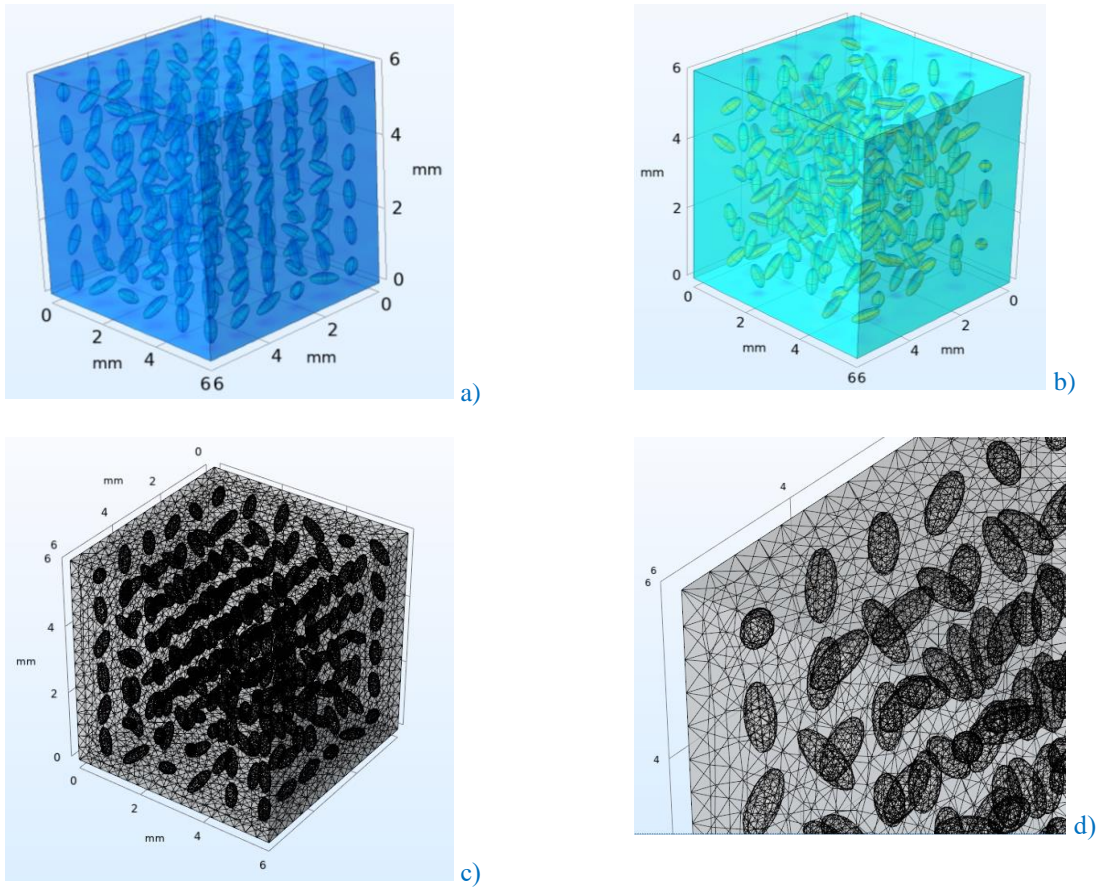
Figure 1. a): ordered distribution of randomly oriented voids in a cube of 6×6×6 mm; b): disordered distribution of randomly 216 oriented voids in a cube of 6×6×6 mm; c): typical mesh used in the analysis of ellipsoidal voids with semi axis of 0.4×0.16×0.16 millimeter; d): zoom of the mesh.
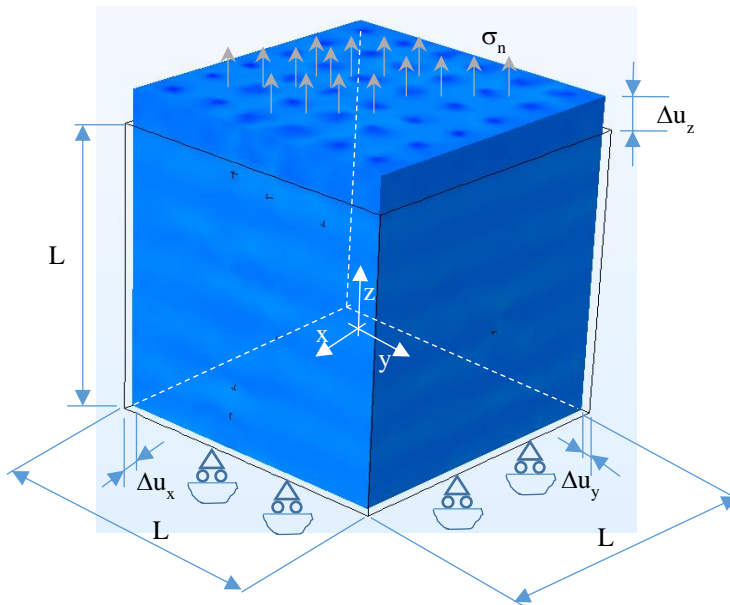
Figure 2. Boundary conditions imposed in FE analysis on a cube with dimensions L×L×L mm (L=6 mm).
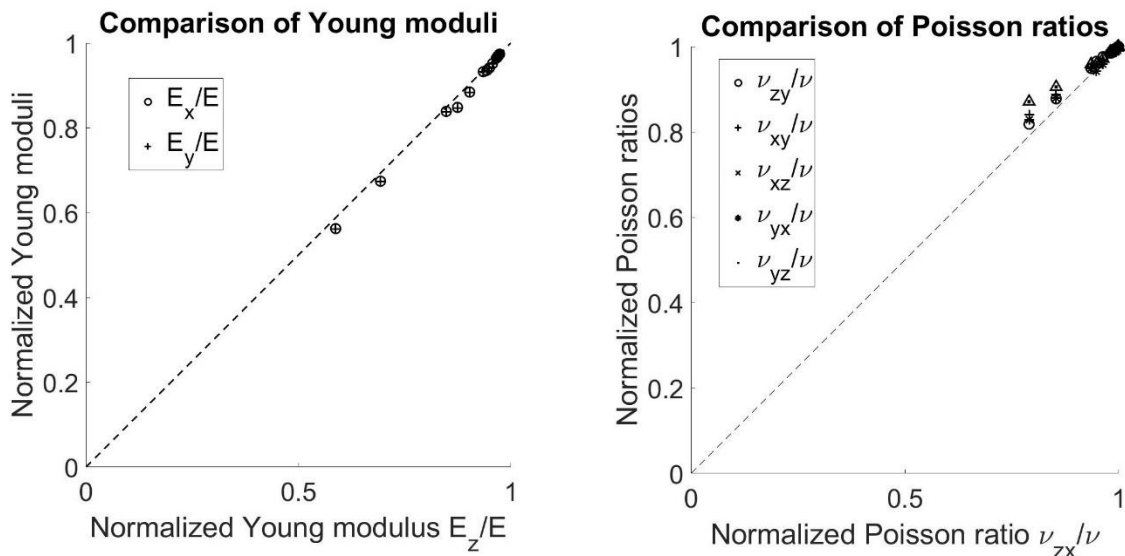

Figure 3. Comparison of average normalized elastic moduli calculated with a FE analysis for random distributions of voids. Left: comparison of Young moduli. Right: comparison of Poisson ratios. The alignment of the data with the 45-degree line indicates isotropic behavior.

Figure 3 shows a comparison between elastic coefficients calculated for random distributions of voids under three uniaxial tensile tests with stress applied along the x, y and z directions, respectively. The plot on the

left-hand side shows a comparison between the Young moduli $\bar{E}_z$, $\bar{E}_x$ and $\bar{E}_y$. The data are quite aligned with the 45-degree line corresponding to the ideal ratio $\bar{E}_x/\bar{E}_z = 1$ ($\bar{E}_y/\bar{E}_z = 1$) indicating isotropic behavior. The plot on the right-hand side of Figure 3 shows a comparison between the six Poisson ratios $\bar{\nu}_{zx}$, $\bar{\nu}_{zy}$, $\bar{\nu}_{xy}$, $\bar{\nu}_{xz}$, $\bar{\nu}_{yx}$ and $\bar{\nu}_{yz}$. The alignment of the data with the straight line inclined at 45 degrees indicates again an almost isotropic behavior for the considered microstructure in the porosity range from zero to 25%. Porosity levels larger than 25%, which are far above the graphite content in gray cast iron (cf. Table 7), are not of interested in the present analysis and thus they have not been investigated. In Figure 3, the lowest values for the Young moduli and the Poisson ratios correspond to the largest values of porosity considered in FE simulations, about 25%. For this porosity level, the normalized Young moduli are found to range from 0.56 to 0.58 (depending on the direction), while the normalized Poisson ratios are found to be higher, ranging from 0.79 to 0.90 (depending on the direction). This difference could be explained as follows. While it is expected that an increase in porosity causes a decrease of the Young moduli, at a rate depending on the voids' aspect ratio, the dependence of the effective Poisson ratios on the porosity is known to be more subtle. In fact, the Poisson ratio is theoretically known to increase, decrease o remain constant with increasing porosity, cf. [28].

2.3. Comparison of results at the microscale

In this Subsection, the elastic parameters calculated via FE analysis are compared with the estimates provided by Equations (1)-(6) and by those given by the rule of mixtures, Equations (11) and (12).

Figure 4 shows a two-dimensional density plot of the normalized average Young's modulus $\bar{E}/E$ versus the porosity λ and the void aspect ratio t. The density plot has been obtained by using Equations (1)-(6), i.e. PW estimate. For comparison, in the same Figure contour lines plotted by using the data obtained from FE simulations are also shown. Dashed line and dotted lines correspond to ordered and disordered voids distributions, respectively. Thick dash-dotted vertical lines correspond to Equation (11) of the rule of mixtures (RM). The main idea behind Figure 4 (and Figures 5, 8 and 9 below) is that the closer the contour lines plotted by using different methods (PW estimate, FE analysis or RM approach), the better the agreement between the used methods. So, representations like the one proposed in Figure 4 allow to evaluate the agreement between the used approaches at a glance, taking into account the dependence on porosity and inclusions aspect ratio.

Deeper inspection of Figure 4 shows also that the average Young modulus is weakly dependent on the porosity aspect ratio, in particular for lower values of porosity and higher aspect ratio. Even though the black (dashed and dotted) curves of the FE estimate do not perfectly overlap with the contour (solid) lines of the density plot given by the PW estimate, the close spacing between them indicates a good agreement between FE analysis and homogenization results, with a better accordance for disordered voids (dotted lines). In contrast, thick dash-dotted vertical lines corresponding to the rule of mixture are well separated from the contour lines of the density plot and shifted to the right, suggesting that RM always provides an overestimate of the Young's modulus, an occurrence already reported in [29].

Tables 1 and 2 show the absolute value of the relative percent errors of the PW estimate vs FE analysis for normalized Young's modulus calculated for ordered and disordered distributions of spheroidal voids, respectively. For ordered distributions, the data confirm the trend of Figure 4, indicating a very good agreement between the two estimates, with a maximum error of 2.69% for ordered distributions and 3.04% for disordered ones. Tables 1 and 2 show also the absolute value of the relative percent errors of the RM estimate vs FE analysis for normalized Young's modulus calculated for ordered and disordered distributions of spheroidal voids, respectively. In this case the errors increase, with a maximum error rises to 23.99% for ordered distributions and 28.87% for disordered ones, confirming that the rule of mixture provides in general a worse estimate with respect to the PW approach. On the other hand, it must be said that the maximum error of the RM estimate is attained for a porosity value of 25%, which is higher than typical values of graphite volume fraction in gray cast iron (about 10-15%).

Figure 5 shows a two-dimensional density plot of the normalized average Poisson's coefficient $\bar{\nu}/\nu$ versus the porosity λ and the void aspect ratio t. As in Figure 4, the density plot has been obtained by using Equations (1)-(6). Figure 5 shows also contour lines plotted by using the data obtained from FE simulations are also shown: dashed line and dotted lines correspond to ordered and disordered voids distributions, respectively. Thick dash-dotted vertical lines correspond to Equation (12) of the rule of mixtures.

As for the Young's modulus, the normalized Poisson's coefficient is weakly dependent on the porosity aspect ratio, in particular for lower values of porosity and higher aspect ratio. The close spacing between the (solid) contour lines calculate via the PW estimate and dashed line and dotted lines obtained by using FE data indicates a good overall agreement. When comparing with Figure 4, in Figure 5 dashed line (FE, ordered) and dotted lines (FE, disordered) corresponding to the same value of the normalized average Poisson's coefficient $\bar{\nu}/\nu$ are shifted left from the corresponding contour lines of PW estimate, indicating that the PW approach provides an inferior (under)estimate for the Poisson's coefficient with respect to the estimate of the Young's modulus. The situation is worse for the RM estimate, for which thick dash-dotted vertical lines located even further left from the contour lines of PW estimate.

The data listed in Tables 3 and 4 are the absolute value of the relative percent errors of the PW estimate vs FE analysis for normalized Poisson's coefficient calculated for ordered and disordered distributions of spheroidal voids, respectively. Inspection of the data reveals that the maximum absolute error is 9.57% for ordered distributions, and 16.07% for disordered ones. These errors are larger than those found for the Young's modulus, indicating that for the Poisson's coefficient the agreement is less pronounced. The data show an even inferior agreement for the RM estimate, with a maximum absolute error of 12.13% for ordered distributions, and 26.07% for disordered ones.
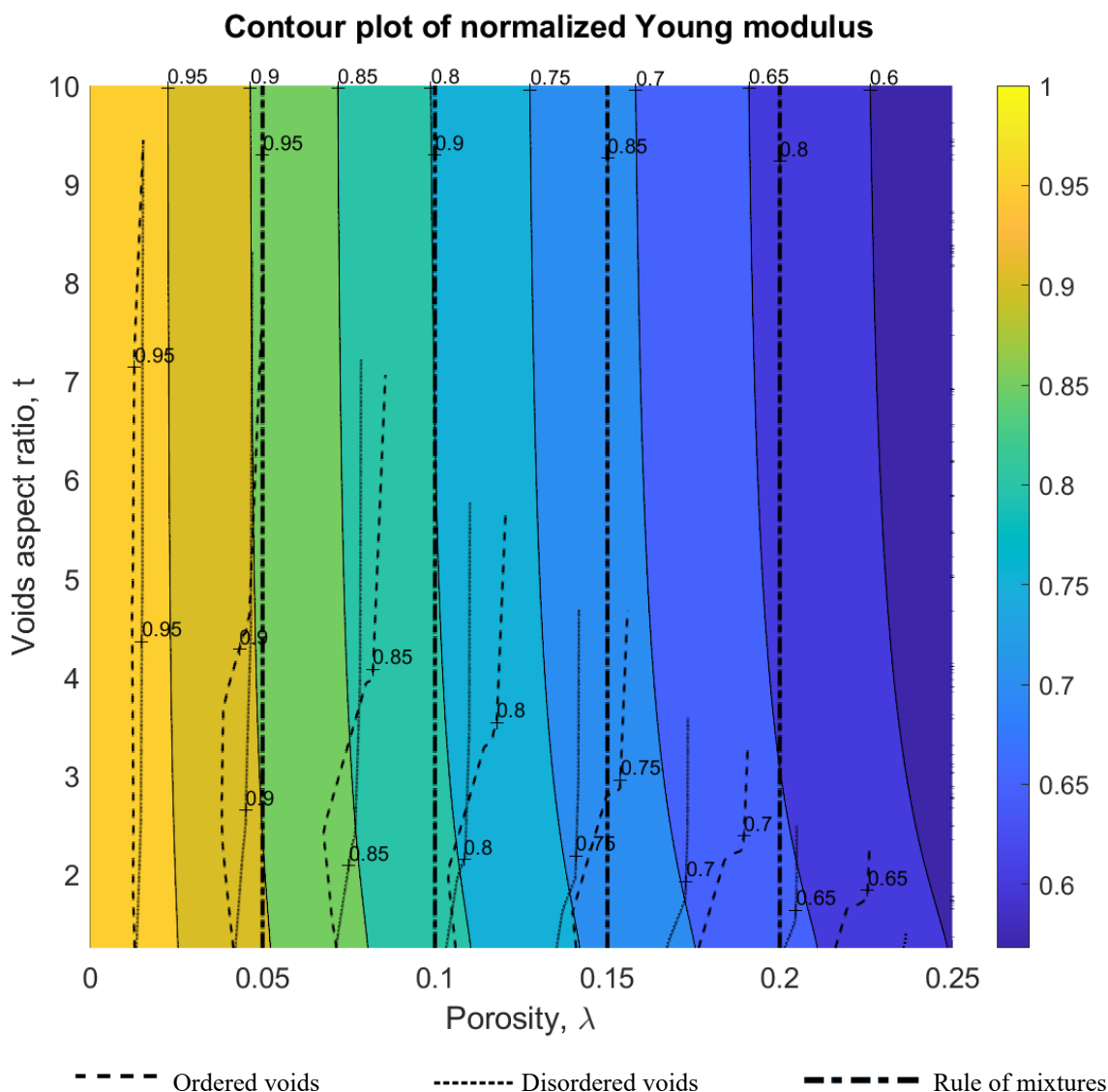
Figure 4. Two-dimensional density plot of normalized average Young's modulus $\bar{E}/E$ versus porosity, λ, and void aspect ratio, t. The density plot has been obtained using the homogenization approach proposed in [PW], the color bar refers to different levels of $\bar{E}/E$. Dashed line and dotted lines are contour plots calculated with FE simulations for ordered and disordered voids distributions, respectively. Thick dash-dotted vertical lines correspond to the rule of mixtures, cf. equation (11). The numbers indicate values over which the contours are drawn.

Error on $\bar{E}/E$ vs. FE, ordered (%)		t									
		1		1.25		2.5		5		10	
		PW	RM	PW	RM	PW	RM	PW	RM	PW	RM
λ	**0-10%**	2.63	5.88	2.65	9.38	2.68	9.33	2.69	4.44	2.69	3.04
	10-20%	0.97	12.44	0.08	17.32	–	–	–	–	–	–
	20-25%	2.32	23.99	1.45	22.99	–	–	–	–	–	–

Table 1. Maximum relative percent errors on the normalized Young's modulus estimated by homogenization analysis (via PW estimate) and by the rule of mixture (RM) vs the results of the FE analysis calculated for ordered distributions of spheroidal voids.

Error on $\bar{E}/E$ vs. FE, disordered (%)		t									
		1		1.25		2.5		5		10	
		PW	RM	PW	RM	PW	RM	PW	RM	PW	RM
λ	0-10%	0.26	10.33	2.65	9.36	2.68	7.34	2.69	3.71	2.69	2.88
	10-20%	1.06	21.87	1.77	19.49	–	–	–	–	–	–
	20-25%	2.99	28.87	3.04	28.59	–	–	–	–	–	–

Table 2. Maximum relative percent errors on the normalized Young's modulus estimated by homogenization analysis (via PW estimate) and by the rule of mixture (RM) vs the results of the FE analysis calculated for disordered distributions of spheroidal voids.
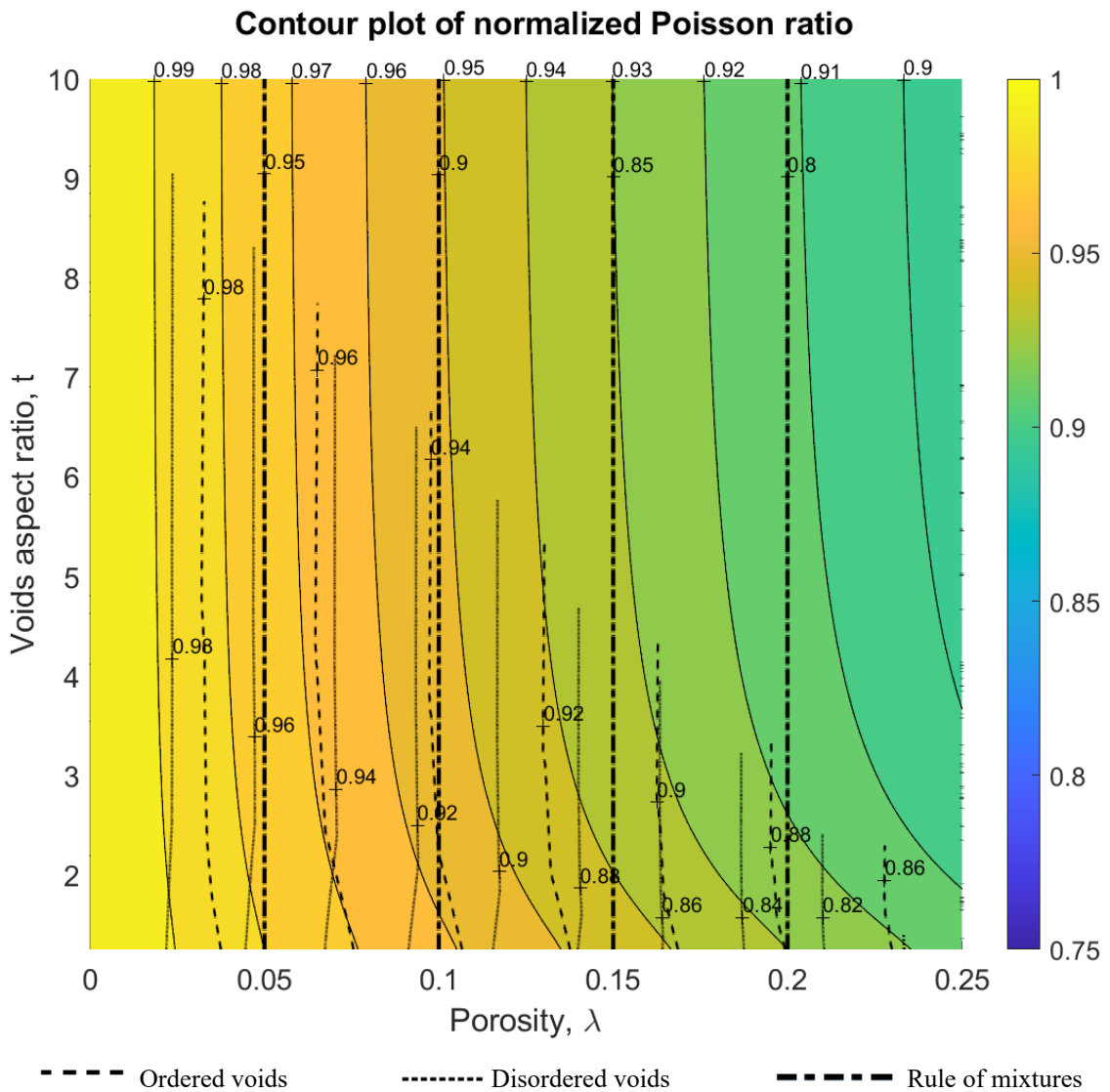

Figure 5. Two-dimensional density plot of normalized average Poisson's ratio $\bar{\nu}/\nu$ versus porosity, λ, and void aspect ratio, t. The density plot has been obtained using the homogenization approach proposed in [PW], the color bar refers to different levels of $\bar{E}/E$. Dashed line and dotted lines are contour plots of $\bar{\nu}_x/\nu$ calculated with FE simulations for ordered and disordered voids distributions, respectively. Thick dash-dotted vertical lines correspond to the rule of mixtures, cf. equation (12). The numbers indicate values over which the contours are drawn.

Error on $\bar{\nu}/\nu$ vs. FE, ordered (%)		t									
		1		1.25		2.5		5		10	
		PW	RM	PW	RM	PW	RM	PW	RM	PW	RM
λ	0-10%	0.56	1.48	0.98	3.59	0.86	2.59	0.17	0.56	0.01	0.16
	10-20%	2.73	4.89	4.50	7.75	–	–	–	–	–	–
	20-25%	9.57	12.13	7.86	11.16	–	–	–	–	–	–

Table 3. Maximum relative percent errors on the normalized Poisson's ratio estimated by homogenization analysis (via PW estimate) and by the rule of mixture (RM) vs the results of the FE analysis calculated for ordered distributions of spheroidal voids.

Error on $\bar{\nu}/\nu$ vs. FE, disordered (%)		t									
		1		1.25		2.5		5		10	
		PW	RM	PW	RM	PW	RM	PW	RM	PW	RM
λ	0-10%	12.76	17.24	3.85	0.85	2.52	0.99	0.50	0.23	0.08	0.09
	10-20%	11.50	23.26	9.91	2.48	–	–	–	–	–	–
	20-25%	10.68	26.07	16.07	4.41	–	–	–	–	–	–

Table 4. Maximum relative percent errors on the normalized Poisson's ratio estimated by homogenization analysis (via PW estimate) and by the rule of mixture (RM) vs the results of the FE analysis calculated for disordered distributions of spheroidal voids.

3. Methods for mesoscale modelling

In the proposed multiscale model (MM), the mesoscale is the scale of the clusters of defects. Each cluster of graphite inclusions is modeled as a spheroidal inclusion made of homogenized material with the average elastic properties calculated in the Section 2. The stress analysis of such a cluster can be analytically performed via Eshelby's solution for an ellipsoidal inclusion perfectly bonded to an infinite elastic three-dimensional matrix under a given remote uniform load σ_0.

A FE analysis has been also performed and two different configurations have been analyzed and compared with the results given by Eshelby's solution: an inclusion embedded in an elastic matrix and made of porous material with equivalent elastic properties; 216 spherical voids placed inside a cluster made of the same material of the matrix.

3.1. Stress analysis based on Eshelby's solution

Eshelby's solution establishes that the stress and strain fields inside a spheroidal inclusion embedded into an elastic matrix are uniform and depending only the elasticity tensors of the matrix and inclusion materials, C_0 and C_1 respectively, on the aspect ratio t of the spheroid and on the applied remote load σ_0 [14,15,16]. In particular, the interior stress σ^{in} takes the form

$$\sigma^{in} = \sigma_0 + C_0[Se^* - e^*], \qquad (13)$$

where S is the Eshelby's tensor and e^* is the equivalent eigenstrain of the inclusion, solution to the equation

$$\sigma_0 + C_0[Se^* - e^*] = C_1\left(C_0^{-1}\sigma_0 + Se^*\right). \qquad (14)$$

The components of the Eshelby's tensor S for a spheroidal inclusion are given in the Appendix.

The stress σ^{out} just outside the inclusion depends on the position on the outer surface of the inclusion, and in particular on the unit outward normal n to the inclusion, as follows:

$$\sigma^{out} = \sigma_{in} + C_0[e^* - (M((C_0 e^*)n)) \otimes n], \tag{15}$$

where the matrix M is given as

$$M = \frac{1}{\mu}\left[I - \frac{1}{2(1-\nu)}(n \otimes n)\right], \tag{16}$$

with μ and ν the shear modulus and the Poisson's ratio of the matrix, respectively, and $\otimes$ indicates the dyadic product between vectors. In this paper, the materials of the matrix and the inclusion are assumed to be isotropic, so the elasticity tensor C_0 and C_1 take the form

$$C = 2\mu\mathbb{I} + \left(\kappa - \frac{2}{3}\mu\right) I \otimes I, \tag{17}$$

where κ and μ are the shear and bulk moduli of the material, respectively, $\mathbb{I}$ is taken to denote the fourth order identity and $\otimes$ the dyadic product between second order tensors.

3.2. Stress analysis based on finite element method

A spheroidal cluster having semiaxes of 6 and 3 mm and embedded into a rectangular box of dimensions 25×25×40 mm has be numerically analyzed in COMSOL. In the model quadratic elements have been used and its number were around $4 \cdot 10^5$. The semiaxes of the cluster are parallel to the edges of the rectangular box. The cluster contains a disordered distribution of small equal spherical voids with radius of 0.4 mm. The material inside and outside the cluster is assumed to be, as before, homogeneous, linear elastic and isotropic, with Young's modulus $E = 206$ GPa and Poisson's ratio $\nu = 0.3$. The rectangular box is subjected to a state of uniaxial traction by imposing a vanishing vertical displacement at the bottom surface of the box and a uniform distributed traction surface load σ_0 at the top surface, as represented in the left-hand side of Figure 6. The numerical analysis performed in COMSOL provides the stress distribution inside and outside the cluster.

The volume-averaged values of the stress components inside the cluster have been normalized with respect to the applied load σ_0 and compared with the normalized, uniform stress components given by Eshelby's solution for an inclusion with homogenized porous material described by Eqns. (1-5). The comparison is illustrated in Subsection 3.3.

For the stress distribution external to the cluster, the values of the load normalized stress components at the outer surface of the cluster have been calculated over the equatorial line of the spheroidal surface of the cluster, represented in the right-hand side of Figure 6. These normalized stress components have been compared with the corresponding ones calculated by using Eshelby's solution at the external surface of the inclusion. The comparison is discussed in Subsection 3.4.

3.3. Comparison of results for internal stress analysis

Table 5 shows the load normalized, volume-averaged stress components calculated with the FE simulation inside the cluster versus the uniform stress components obtained by injecting Eqns. (1-5) into Eqn. (13). Inspection of data listed in Table 5 shows an overall good agreement between the two sets of stress components. Two additional cluster orientations were also considered in the analysis: a cluster rotated of 45° about the y-axis indicated in Figure 6 and a cluster rotated of 90° about the same axis. For these new orientations, the agreement between the internal stress components from FE simulation and from the multiscale model confirmed to be very good. To avoid redundancy, the corresponding data are not presented.

Model	$\sigma_{xx}^{in}/\sigma_0$	$\sigma_{yy}^{in}/\sigma_0$	$\sigma_{zz}^{in}/\sigma_0$	$\sigma_{xy}^{in}/\sigma_0$	$\sigma_{xz}^{in}/\sigma_0$	$\sigma_{yz}^{in}/\sigma_0$
FE	0.018	0.001	0.770	0.001	0.000	-0.001
MM	0.018	0.001	0.779	0.000	0.000	0.000

Table 5. Load normalized, volume-averaged, internal stress components calculated via a FE analysis of a traction test performed over a box including a porous cluster (label "FE") vs the same uniform components calculated by using the multiscale model (label "MM"), i.e. Eshelby's solution for an inclusion of equivalent homogenized porous material.
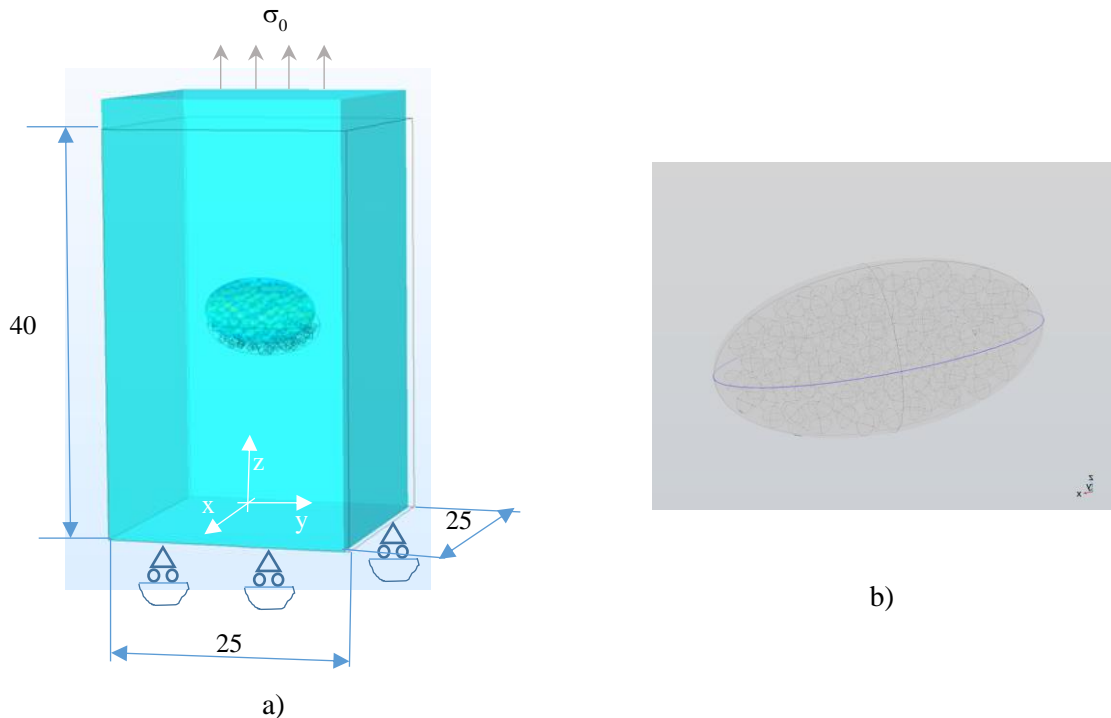
Figure 6. a): configuration used in COMSOL for the stress analysis: a spheroidal inclusion with semiaxes of 6 and 3 mm incorporating spheroidal voids with radius of 0.4 mm. b): equatorial line of the external surface of the cluster on which the outer stresses have been calculated. Note that some voids could slightly intersect the surface of the spheroid (size in millimeters).

3.4. Comparison of results for external stress analysis

Figure 7 shows the plots of distribution of outer stress components over the equatorial line of the spheroidal surface of the cluster calculated using the two different approach, i.e. the FE method and the multi-scale model (MM) In the plots, the values of the stress components are normalized with respect to the applied load σ_0. The plots indicate that the multiscale model is able to capture the average trend of the distributions calculated using the FE method. This is confirmed by Table 2 in [29], where a good agreement between the average values (averaged along the equatorial lines of the cluster) of the stress components calculated using the multiscale method and FE analysis has been found. Disagreement between the curves in Figure 7 is due stress peaks in FE data, given by the presence of neighboring cavities close to the surface of the cluster. These peaks, correctly reproduced by the FE model, are completely lacking in the curves obtained using the multiscale model, which appear to be more regular. The reason is that in the multiscale model defects internal to the cluster are smeared out into equivalent porosity, and thus local stress peaks cannot be taken into

account. This aspect represents a main drawback of the multiscale model, in view of the fact that stress peaks may lead to cracking and fracture.
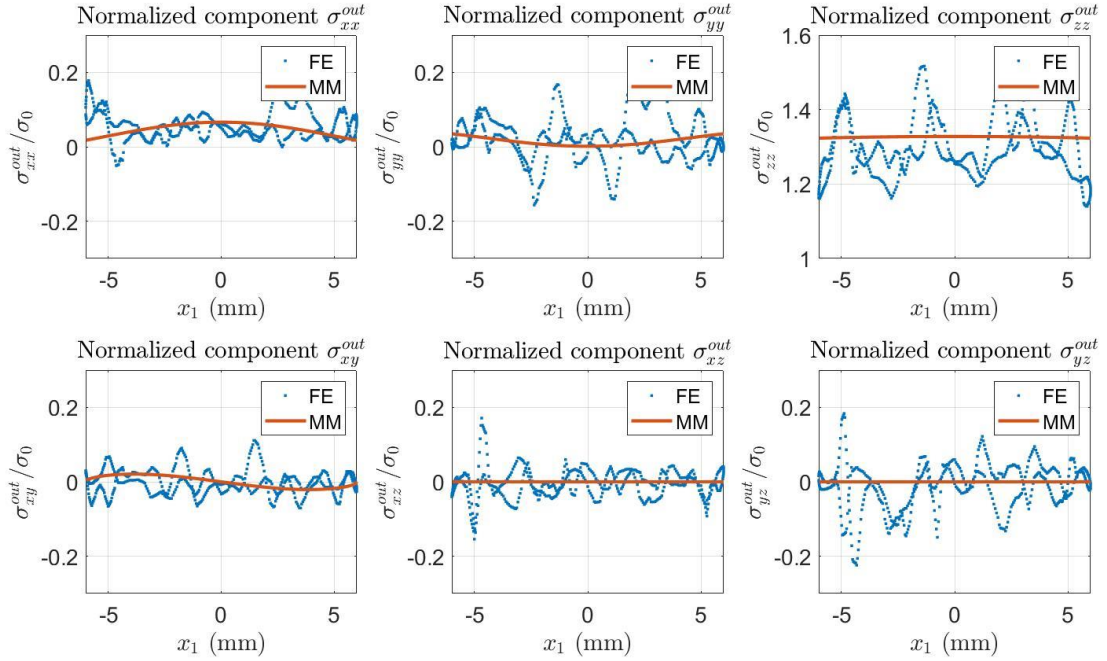

Figure 7. Comparison between stress distributions over the equatorial line at the outer surface of the cluster calculated using the finite element method (label "FE") and by using the multiscale model (label "MM"), i.e. Eshelby's solution for an inclusion of equivalent homogenized porous material.

3.5. Estimates of stress concentration factors

Using Eqns. (13) and (17) together with the estimates for the elastic constants of the porous material provided by Eqn. (1)-(5), it is possible to calculate the stress concentration factors at the interior and on the outer surface of the inclusion modelling the cluster of degenerated graphite.

A MATLAB routine has been implemented to calculate the components of stress tensors σ^{in} and σ^{out}, and in particular their eigenvalues, denoted $\sigma_k^{in}, k = 1, 2, 3$ for the inner stress and $\sigma_k^{out}, k = 1, 2, 3$ for the outer one. Because the internal stress components are uniform in Eshelby's solution, the inner stress concentration factor, SCF^{in}, is defined as

$$SCF^{in} = max\left\{\frac{\sigma_1^{in}}{\sigma_0}, \frac{\sigma_2^{in}}{\sigma_0}, \frac{\sigma_3^{in}}{\sigma_0}\right\} \tag{18}.$$

The outer stress components are found to depend upon the position on the outer surface of the spheroid. It is convenient to introduce an angular spheroidal coordinates with $\vartheta \in [0, \pi)$ the angle formed by the position vector of a generic point on the spheroidal surface and the spheroid's, and $\varphi \in [0, 2\pi)$ the azimuthal angle of the position vector, i.e. the angle of rotation from the initial meridian plane. Then, the concentration factor, SCF^{out}, is defined as

$$SCF^{out} = max_{\substack{\vartheta \in [0,\pi) \\ \varphi \in [0,2\pi)}} \left\{\frac{\sigma_1^{out}(\vartheta,\varphi)}{\sigma_0}, \frac{\sigma_2^{out}(\vartheta,\varphi)}{\sigma_0}, \frac{\sigma_3^{out}(\vartheta,\varphi)}{\sigma_0}\right\} \tag{19}.$$
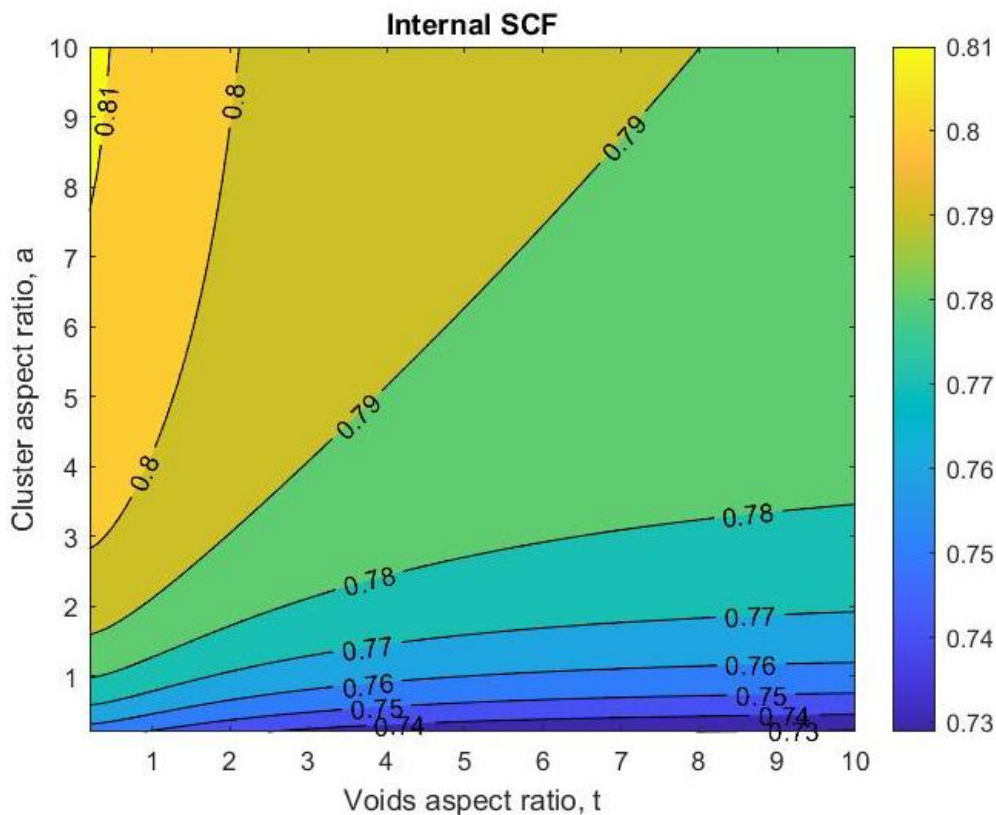
Figure 8. Density plot of the internal stress concentration factor, defined as in Eqn. (18), versus cluster aspect ratio, a, and void aspect ratio, t. A porosity value of 25% has been assumed.
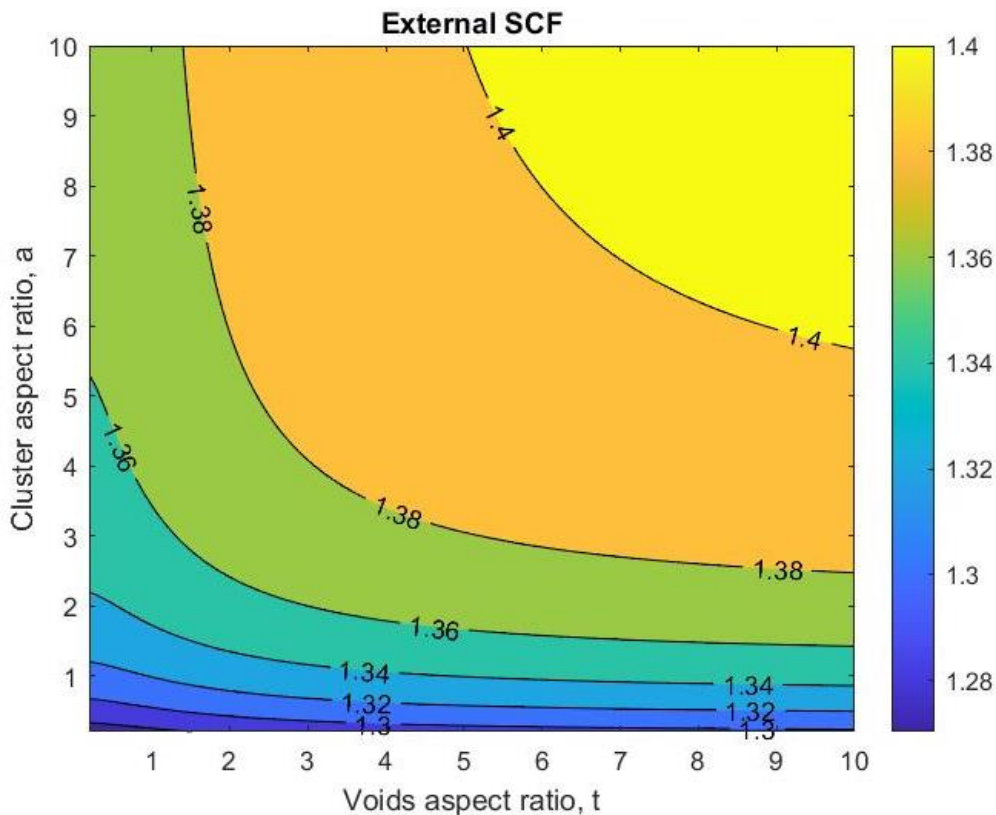

Figure 9. Density plot of the external stress concentration factor, defined as in Eqn. (19), versus cluster aspect ratio, a, and void aspect ratio, t. A porosity value of 25% has been assumed.

Given the elasticity parameters of the matrix, chosen as before $E = 206$ GPa and $v = 0.3$, Figures 8 and 9 show the two-dimensional contour plots for the two stress concentration factors in the (t, a) plane, with t the voids' aspect ratio and a the inclusion (or cluster) aspect ratio. In the two figures, a porosity value of 25% has been assumed. As expected, SCF^{out} values are larger than SCF^{in} values. Moreover, while SCF^{in} is found to increase with decreasing t and increasing a, SCF^{out} increases for increasing both t and a, i.e. for slender rod-like voids forming slender aggregates.

4. Comparison of homogenization results with experimental data from literature

In this Section, we compare the proposed analytical and numerical estimates of homogenized elastic properties calculated in Section 2 with some experimental results obtained in [30,31].

In [30], beams constituted of porous material characterized by spherical porosity have been experimentally characterized. In particular, 20×20×150 mm beams made of high strength hemihydrate plaster containing randomly distributed polystyrene spherical agglomerates have been tested in four-point bending conditions. The content of polystyrene has been varied to realize different levels of porosity. The obtained microstructures have been characterized by X-ray computed tomography and optical imaging on bidimensional sections, revealing a random distribution of spherical defects. Figure 10 shows the model used in the FE analysis in the case of porosity of 15%. The load-displacement responses obtained in four-point bending test conditions have shown a quasi-brittle behavior. The Young modulus E, normalized with respect the elastic modulus E_0 of the matrix material, is experimentally found to linearly decrease with porosity increase, accordingly to the following experimental estimate valid up to a porosity of 30%:

$$E/E_0 = 1 - 1.96 \lambda. \tag{20}$$

Table 6 compares the values of the normalized Young modulus calculated with Eqn.(20) at different level of porosity with the estimates obtained with the finite element analysis (FE) and with the homogenized approach proposed by Pan and Weng (PW). The values in the Table indicate that the numerical and theorical estimates are very close and both in good agreement with experimental data, with relative errors lower that 10% for porosity levels up to 20%. For larger porosity levels, relative errors are expected to increase due to the deviation of the real porosity geometry from the idealized distribution of spherical voids considered in calculating the FE and PW estimates.

In [31], the Young's modulus of nodular cast iron $\bar{E}_{ci}$ was obtained by using a pulse-echo elastic-wave technique. Several material samples were examined: specimens I, characterized by lower carbon gray cast iron, were obtained from the jamb of a coke-oven door; specimens II, presenting a higher carbon gray cast iron, were obtained from an ingot mold. Because of variations in graphite flake size and amount due to differential cooling rate during casting, the samples were extracted from two representative locations (labelled A and B) from each of the gray cast irons. Quantitative metallographic techniques were applied to determine the average volume fraction and the average aspect ratio of the graphite flakes. Figure 11 shows the model used in the FE analysis in the case IB. The graphite was modeled by means of thin ellipsoid of revolution.

Table 7 shows the measured values of the Young's modulus, obtained from rod specimens for samples IA and IB, and from thick plate specimens for samples IIA and IIB. In the same Table, the corresponding values provided by the Pan and Weng (PW) estimate and by the numerical analysis (FE) have been listed. The PW and FE estimates have been obtained by considering levels of porosity equal to the measured values of graphite volume fraction. For the considered values of the latter, the data listed in Table 7 indicate a good agreement between the experimental data and the analytical and numerical results.

		Porosity λ (%)				
		5	**10**	**15**	**20**	**25**
E/E_0	**Eqn. (20)**	0.90	0.80	0.71	0.61	0.51
	FE	0.90	0.82	0.73	0.66	0.58
	PW	0.90	0.82	0.74	0.67	0.60

Table 6. Normalized Young's modulus vs. porosity in a porous material: comparison of Pan and Weng [22] estimate and finite element (FE) analysis prediction with the interpolation (Eqn. (20)) of experimental values obtained in [30].

Type of sample	Graphite (%)	Aspect ratio	$\bar{E}_{ci}$ [SSK] (GPa)	PW (GPa)	FE (GPa)	Error TW (%)	Error FE (%)
IA	8.2	14.6	128	128.2	107.9	0.1	15.6
IB	7.1	15.2	134	134.1	119.4	0.1	10.9
IIA	12.7	23.9	97.2	80.8	–	16.9	–
IIB	10.8	24.6	83.4	88.7	–	6.4	–

Table 7. Average Young's modulus vs. porosity in gray cast iron: comparison of Pan and Weng [22] estimate and finite element (FE) analysis prediction with experimental data obtained in [31].
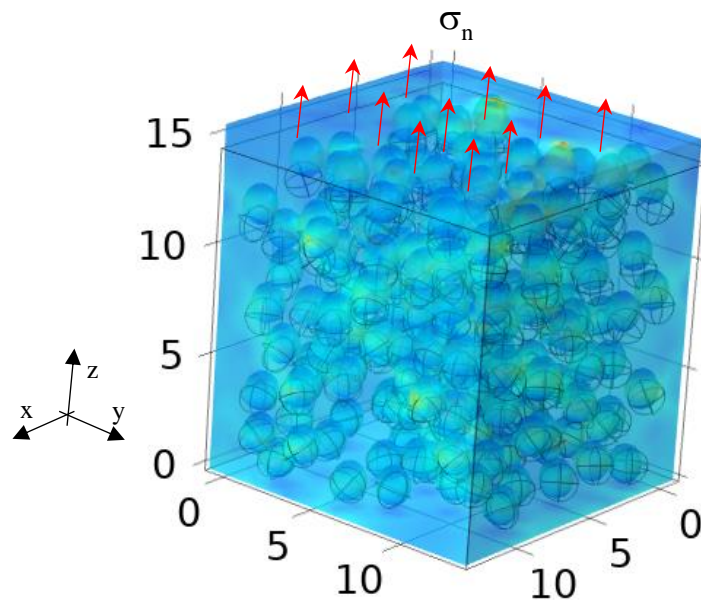

Figure 10. Model used for analyzing the experimental data proposed in reference [30]; porosity of 15% obtained with 216 spherical voids of radius 0.8 mm in a cube of 14.6×14.6×14.6 mm; boundary condition as in Figure 2.
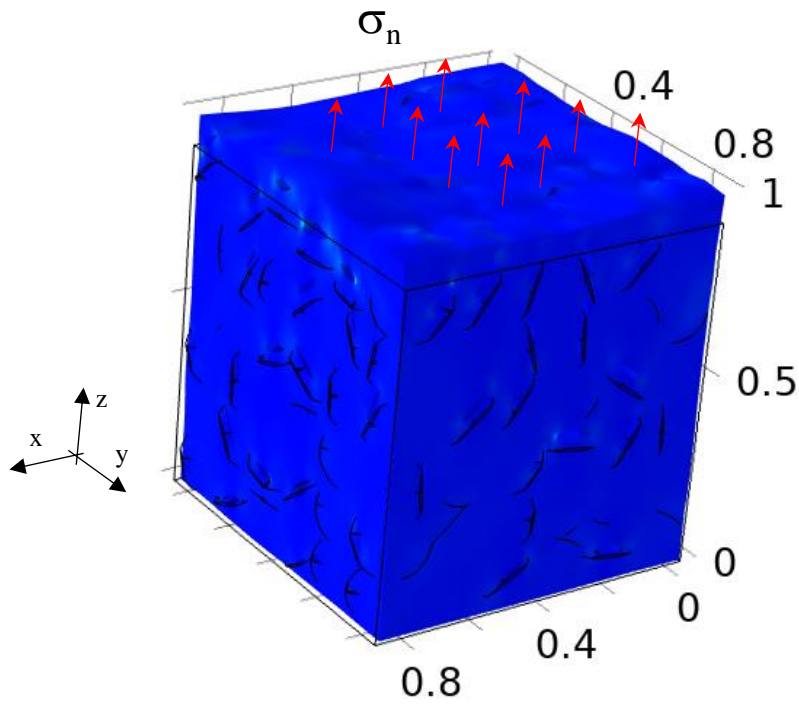
Figure 11. Model used for analyzing the experimental data proposed in reference [31]; Case IB with thin 216 ellipsoidal voids with diameter of 0.19 mm and thickness of 0.013 in a cube of 0.92×0.92×0.92 mm; boundary condition as in Figure 2.

5. Conclusions

The paper proposes a two-scale model for clusters of degenerated graphite in gray cast iron. The graphite precipitates are modeled as spheroidal voids aggregating in a spheroidal cluster embedded in a three-dimensional infinite elastic matrix. At the microscale, the Pan and Weng's estimate for ellipsoidal defects randomly distributed in an elastic matrix is applied to calculate the equivalent elastic constants of the porous material inside the cluster. At the mesoscale, Eshelby's solution is used to calculate the stress components at points internal and external to the cluster, assumed to be composed of the equivalent porous material.

To validate the two-scale model, a finite element analysis has been conducted on random microstructures embedding spheroidal randomly oriented and randomly distributed cavities aggregated in a cluster. The validation at the microscale indicates good agreement between the equivalent elastic properties of the porous material calculated by using Pan and Weng's approach and those calculated by means of the finite element analysis. At the mesoscale, a very good agreement has been found between the internal (uniform) stress components calculated by using Eshelby's solution and the corresponding average stress components calculated via the finite element simulation. A good agreement is also found for the outer stress distribution between the components calculated numerically and using the two-scale model. As expected, the latter is not able to capture stress peaks due to cavities close to the cluster surface, which are smeared out as an equivalent porous material in the two-scale model.

As a second validation, the two-scale model and the numerical approach are validated by comparing the predicted average elastic properties of the porous material inside the clusters with experimental data obtained from the literature [30,31]. Again a good agreement is observed, indicating that analytical or numerical homogenization procedures are effective in estimating the elastic properties of porous materials and in particular of gray cast iron.

Future developments of the present work could address the bonding and the damage of the graphite particles at the interface with the matrix, using approaches similar to those proposed in [32,33,34,35]. Another important aspect could be the validation of the model against experimental data collected by means of X-ray tomography, X-ray diffraction, and digital volume correlation, whose recent developments offer enormous potential [36].

References

[1] Brocks W., Hao S. and Steglich D., 1996. Micromechanical Modelling of the Damage and Toughness Behaviour of Nodular Cast Iron Materials J. Phys. VI 6, 43. https://doi.org/10.1051/jp4:1996605

[2] Bonora N. and Ruggiero A., 2005. Micromechanical modeling of ductile cast iron incorporating damage. Part I: Ferritic ductile cast iron International Journal of Solids and Structures 42, 1401. https://doi.org/10.1016/j.ijsolstr.2004.07.025

[3] Collini L. and Nicoletto G., 2005 Determination of the relationship between microstructure and constitutive behaviour of nodular cast iron with a unit cell model, Journal of Strain Analysis for Engineering Design, 40 (2), 107. https://doi.org/10.1243/030932405X7692

[4] Andriollo T., Thorborg J. and Hattel J., 2016. Modeling the elastic behavior of ductile cast iron including anisotropy in the graphite nodules, International Journal of Solids and Structures Vol. 100–101, 523. https://doi.org/10.1016/j.ijsolstr.2016.09.023

[5] Dong M., Prioul C. and François D., 1997. Damage effect on the fracture toughness of nodular cast iron: Part I. Damage characterization and plastic flow stress modeling, Metallurgical and Materials Transactions A 28, 2245. https://doi.org/10.1007/s11661-997-0182-7

[6] Baer, W., 2020. Chunky Graphite in Ferritic Spheroidal Graphite Cast Iron: Formation, Prevention, Characterization, Impact on Properties: An Overview. Inter. Metalcast. 14, 454. https://doi.org/10.1007/s40962-019-00363-8

[7] Boccaccini A.R., 1997. Young's modulus of cast-iron as a function of volume content, shape and orientation of graphite inclusions, Zeitschrift für Metallkunde 88 (1), 23. https://doi.org/10.3139/ijmr-1997-0005

[8] Rausch, T., Beiss, P., Broeckmann, C., Lindlohr, S., Weber, R., 2010. Application of quantitative image analysis of graphite structures for the fatigue strength estimation of cast iron materials. Procedia Engineering 2(1), 1283. https://doi.org/10.1016/j.proeng.2010.03.139

[9] Costa, N., Machado, N., Silva, F., 2010. A new method for prediction of nodular cast iron fatigue limit, Internal Journal of Fatigue 32 (7), 988. https://doi.org/10.1016/j.ijfatigue.2009.11.005

[10] Mottitschka, T., Pusch, G., Biermann, H., Zybell, L., Kuna, M., 2012. Influence of graphite spherical size on fatigue behaviour and fracture toughness of ductile cast iron EN-GJS-400-18LT. International Journal of Materials Research 103(1), 87. https://doi.org/10.3139/146.110636

[11] Hütter, G., Zybell, L., Kuna, M., 2015. Micromechanisms of fracture in nodular cast iron: From experimental findings towards modeling strategies -A review. Engineering Fracture Mechanics 144, 118. https://doi.org/10.1016/j.engfracmech.2015.06.042

[12] Cova M., Livieri P., Rizzoni R., Tovo R., 2017. A preliminary investigation of strength models for degenerate graphite clusters in grey cast iron. Procedia Structural Integrity 7, 446. https://doi.org/10.1016/j.prostr.2017.11.111

[13] Rizzoni R, Livieri P, Tovo R, Cova M, 2020 Development of a hierarchical model for voids clusters suitable for cast iron degenerated graphite. Theoretical and Applied Fracture Mechanics 109, 102731. https://doi.org/10.1016/j.tafmec.2020.102731

[14] Eshelby J.D., 1957. The determination of the elastic field of an ellipsoidal inclusion, and related problems. Proceedings of the Royal Society of London. Series A, Mathematical and Physical Sciences 241, 376. https://doi.org/10.1098/rspa.1957.0133

[15] Eshelby J.D., 1959. The elastic field outside an ellipsoidal inclusion. Proceedings of the Royal Society of London. Series A, Mathematical and Physical Sciences 252, 561. https://doi.org/10.1098/rspa.1959.0173

[16] Eshelby J.D., 1964. Elastic Inclusions and Inhomogeneities. Progress in Solid Mechanics, eds. N Sneddon and R Hill (Amsterdam: North-Holland) vol. 289–140. Amsterdam: North-Holland.

[17] Hill, R., 1963. Elastic properties of reinforced solids: some theoretical principles, Journal of the Mechanics and Physics of Solids 11, 357. https://doi.org/10.1016/0022-5096(63)90036-X

[18] Hill R., 1965. A self-consistent mechanics of composite materials. Journal of the Mechanics and Physics of Solids s 13, 213. https://doi.org/10.1016/0022-5096(65)90010-4

[19] Mori T., Tanaka K., 1973. Average stress in the matrix and average elastic energy of materials with misfitting inclusions, Acta Metallurgica 21, 571. https://doi.org/10.1016/0001-6160(73)90064-3

[20] Tucker III CL, Liang E., 1999. Stiffness predictions for unidirectional short-fiber composites: review and evaluation, Composite Science and Technology 59, 655. https://doi.org/10.1016/S0266-3538(98)00120-1

[21] Ghossein E., Lévesque M., 2014. A comprehensive validation of analytical homogenization models: the case of ellipsoidal particles reinforced composites, Mechanics of Materials 75, 135. https://doi.org/10.1016/j.mechmat.2014.03.014

[22] Pan H.H., Weng G.J., 1996. Elastic moduli of heterogeneous solids with ellipsoidal inclusions and elliptic cracks. Acta Mechanica 110, 73.

[23] Firooz, S., Steinmann, P., and Javili, A., 2021. Homogenization of Composites With Extended General Interfaces: Comprehensive Review and Unified Modeling, ASME. Appl. Mech. Rev. 73(4), 040802. https://doi.org/10.1115/1.4051481

[24] Tandon G.P., Weng G.J., 1984. The effect of aspect ratio of inclusions on the elastic properties of unidirectionally aligned composites, Polymer Composites 5(4), 327. https://doi.org/10.1002/pc.750050413

[25] Tandon G.P., Weng G.J., 1986. Stress Distribution in and Around Spheroidal Inclusions and Voids at Finite Concentration. ASME Journal of Applied Mechanics 53(3): 511. https://doi.org/10.1115/1.3171804

[26] Tandon G.P., Weng G.J. , 1986. Average stress in the matrix and effective moduli of randomly oriented composites, Composites Science and Technology 27, 111. https://doi.org/10.1016/0266-3538(86)90067-9

[27] Weng G.J., 1984. Some elastic properties of reinforced solids, with special reference to isotropic ones containing spherical inclusions. International Journal of Engineering Science 22 (7), 845. https://doi.org/10.1016/0020-7225(84)90033-8

[28] Lutz M. P., Zimmerman R. W., 2021. The effect of pore shape on the Poisson ratio of porous materials. Mathematics and Mechanics of Solids 26(8), 1191-1203. https://doi.org/10.1177/10812865211023535

[29] Rizzoni R, Livieri P, Tovo R, 2022. Multiscale stress analysis of porosity clusters as mechanical models of degenerated graphite defects in cast iron, IOP Conf. Series: Materials Science and Engineering 1214, 012035. https://doi.org/10.1088/1757-899X/1214/1/012035

[30] Liu D, Šavija B, Smith G E et al. 2017, Towards understanding the influence of porosity on mechanical and fracture behaviour of quasi-brittle materials: experiments and modelling, International Journal of Fracture 205, 57. https://doi.org/10.1007/s10704-017-0181-7

[31] Speich G.R., Schwoeble A.J. and Kapadia B.M., 1980, Elastic Moduli of Gray and Nodular Cast Iron, ASME Journal of Applied Mechanics 47, 821. https://doi.org/10.1115/1.3153797

[32] Lebon F., Dumont S., Rizzoni R., López-Realpozo J.C., Guinovart-Díaz R., Rodríguez-Ramos R., Bravo-Castillero J., Sabina F.J., 2016. Soft and hard anisotropic interface in composite materials, Composites Part B: Engineering, 90, 58. https://doi.org/10.1016/j.compositesb.2015.12.003

[33] Bonetti E., Bonfanti G., Lebon F., Rizzoni R, 2017. A model of imperfect interface with damage, Meccanica, 52 (8), 1911. https://doi.org/10.1007/s11012-016-0520-1

[34] Guinovart-Sanjuán D., Rizzoni R., Rodríguez-Ramos R., Guinovart-Díaz R., Bravo-Castillero J., Alfonso-Rodríguez R., Lebon F., Dumont S., Sevostianov I., Sabina F.J, 2017. Behavior of laminated shell composite with imperfect contact between the layers, Composite Structures, 176, 539. https://doi.org/10.1016/j.compstruct.2017.05.058

[35] Livieri P., Tovo T., 2017. Analysis of the thickness effect in thin steel welded structures under uniaxial fatigue loading, International Journal of Fatigue 101 (2), 363. https://doi.org/10.1016/j.ijfatigue.2017.02.011

[36] Andriollo T., Xu C., Zhang Y., Tiedje N.S., Hattel J., 2021. Recent trends in X-ray-based characterization of nodular cast iron. Mat. Design Process. Comm. 2021; 3:e212. https://doi.org/10.1002/mdp2.212

Appendix

Components of the Eshelby's tensor for a spheroidal inclusion:

$$S_{1111} = (1 - 2\nu_0 + (3t^2 - 1)/(t^2 - 1) - g(1 - 2\nu_0 + 3t^2/(t^2 - 1)))/(2(1 - \nu_0))$$
$$S_{2222} = 3\,t^2/(8(1 - \nu_0)(t^2 - 1)) + g\,(1 - 2\nu_0 - 9/(4(t^2 - 1)))/(4(1 - \nu_0))$$
$$S_{3333} = 3\,t^2/(8(1 - \nu_0)(t^2 - 1)) + g\,(1 - 2\nu_0 - 9/(4(t^2 - 1)))/(4(1 - \nu_0))$$
$$S_{2233} = (t^2/(2(t^2 - 1)) - g(1 - 2\nu_0 + 3/(4(t^2 - 1))))/(4(1 - \nu_0))$$
$$S_{3322} = (t^2/(2(t^2 - 1)) - g(1 - 2\nu_0 + 3/(4(t^2 - 1))))/(4(1 - \nu_0))$$
$$S_{2211} = -t^2/(2(1 - \nu_0)(t^2 - 1)) + g\,(3t^2/(t^2 - 1) - (1 - 2\nu_0))/(4(1 - \nu_0))$$
$$S_{3311} = -t^2/(2(1 - \nu_0)(t^2 - 1)) + g\,(3t^2/(t^2 - 1) - (1 - 2\nu_0))/(4(1 - \nu_0))$$
$$S_{1122} = S_{1133} = -(1 - 2\nu_0 + 1/(t^2 - 1))/(2(1 - \nu_0)) + g\,(1 - 2\nu_0 + 3/(2(t^2 - 1)))/(2(1 - \nu_0))$$
$$S_{2323} = S_{3232} = (t^2/(2(t^2 - 1)) + g(1 - 2\nu_0 - 3/(4(t^2 - 1))))/(4(1 - \nu_0))$$
$$S_{1212} = S_{1313} = (1 - 2\nu_0 - (t^2 + 1)/(t^2 - 1) - (g/2)(1 - 2\nu_0 - (3(t^2 + 1))/(t^2 - 1)))/(4(1 - \nu_0))$$

where ν_0 is the Poisson ratio of the matrix, t is the aspect ratio of the inclusion (length to diameter) and g is given by

$$g = t\,(t(t^2 - 1)^{\frac{1}{2}} - \text{ArcCosh}(t))/(t^2 - 1)^{3/2}$$

for a prolate shape $(t > 1)$ and

$$g = t\,(\text{ArcCos}(t) - t(t^2 - 1)^{\frac{1}{2}})/(t^2 - 1)^{3/2}$$

for an oblate shape $(t < 1)$. For a spherical inclusion $(t = 1)$, the above relations simplify into

$$S_{1111} = S_{2222} = S_{3333} = \frac{7 - 5\nu_0}{15(1 - \nu_0)}$$

$$S_{1122} = S_{2233} = S_{3311} = \frac{5\nu_0 - 1}{15(1 - \nu_0)}$$

$$S_{1212} = S_{2323} = S_{3131} = \frac{4 - 5\nu_0}{15(1 - \nu_0)}$$

.